NJC

ROYAL SOCIETY OF CHEMISTRY

PAPER

View Article Online
View Journal | View Issue

Check for updates

Cite this: *New J. Chem.*, 2025, **49**, 7035

Theoretical study on vertical $B_2CSe/Mg(OH)_2$ van der Waals heterostructures with high solar-to-hydrogen efficiency†

Francis Opoku, *[ac] Eric Selorm Agorku, [a] Samuel Osei-Bonsu Oppong, [b] Edward Ebow Kwaansa-Ansah, [a] Noah Kyame Asare-Donkor [a] and Penny Poomani Govender *[c]

The search for efficient and stable photocatalysts for solar-driven water splitting remains a critical challenge in renewable energy research. In this study, the $B_2CSe/Mg(OH)_2$ van der Waals heterostructure (vdWH) was investigated as a promising candidate using first-principles simulations. The heterostructure demonstrated exceptional thermal, kinetic, and mechanical stability, as confirmed through *ab initio* molecular dynamics, phonon dispersion, and mechanical property analyses. The $B_2CSe/Mg(OH)_2$ vdWH exhibited a reduced indirect bandgap compared to the $Mg(OH)_2$ monolayer, facilitating efficient photogenerated electron–hole pair separation. A type-II band alignment, supported by charge density difference, electronic structure, and built-in electric field analyses, further enhanced redox capacity and carrier separation efficiency. The heterostructure achieved a remarkable solar-to-hydrogen (STH) conversion efficiency of 34.58%, outperforming many existing systems, and demonstrated strong optical absorption across the visible light spectrum. Strain engineering revealed the potential for adaptive photocatalyst design, with compressive strain inducing a transition from type-II to type-I band alignment and tensile strain effectively redshifting the absorption edge to harness a broader range of solar energy. This tunability allows for precise control over the electronic and optical properties of the heterostructure, enabling optimization for specific photocatalytic applications. A potential drop of 8.06 eV across the interface and a charge transfer of 0.0045 electrons from $Mg(OH)_2$ to B_2CSe further enhanced the heterostructure's photocatalytic potential. These findings not only highlight the $B_2CSe/Mg(OH)_2$ vdWH as a highly efficient and stable photocatalyst for overall water splitting but also underscore the transformative role of strain engineering in designing adaptive photocatalysts. This approach offers a promising pathway for advancing solar energy utilization and hydrogen production, paving the way for next-generation renewable energy technologies.

Received 20th February 2025,
Accepted 24th March 2025

DOI: 10.1039/d5nj00757g

rsc.li/njc

I. Introduction

Environmental degradation and the energy crisis are caused by the steady depletion of non-renewable energy resources due to population growth. Hydrogen (H_2) is a promising energy carrier to settle the current energy crisis and environmental contamination[1] because of its high energy density, superior calorific value, clean and carbon-neutral fuels and chemicals.[2–4] Among all the H_2 production techniques, photocatalytic H_2 production from water is a viable approach for low-cost, direct and clean energy harvesting[5] as it can directly produce H_2 from water using sunlight or visible light.[6–8] Over the past 40 years, a number of materials have demonstrated potential photocatalytic applications.[9,10] It is generally recognized that a photocatalytic water splitting application should have a proper bandgap and band alignment to have a high redox capacity.[11] Among the several visible-light photocatalysts studied, inorganic semiconductor materials have received considerable attention from researchers.[12] Two-dimensional (2D) materials offer notable advantages over bulk materials based on water splitting because of their high electronic and optical properties, large surface area, numerous active sites, and catalytically active layered structural features.[11,13–15]

Since a mechanical stripping process was used to prepare graphene,[16] significant research efforts are now focused on investigating 2D materials with remarkable physicochemical

---

[a] *Department of Chemistry, Kwame Nkrumah University of Science and Technology, Kumasi, Ghana. E-mail: ofrancis2010@gmail.com, francisopoku@knust.edu.gh*
[b] *Marine Engineering Department, Regional Maritime University, P. O. Box 1115, GP Accra, Ghana*
[c] *Department of Chemical Sciences, Doornfontein Campus, University of Johannesburg, P. O. Box 17011, Johannesburg, 2028, South Africa. E-mail: pennyg@uj.ac.za*

† Electronic supplementary information (ESI) available. See DOI: https://doi.org/10.1039/d5nj00757g

properties, such as high carrier mobility, mechanical stability, and excellent optical and electronic properties, in several possible device applications. Among the popular layered semiconductor materials are transition metal dichalcogenide materials, which have superior optical-,[17] thermal-[18] and electronic[19] properties. By predicting 2D materials, new intriguing characteristics were created, allowing these stacked materials to be expanded.[20–22] More recently, it was revealed that monolayered $Mg(OH)_2$ with stable chemical and vibrational characteristics were created using the hydrothermal crystal formation method. These sheets could be used as flexible optoelectronics.[23] Interestingly, $Mg(OH)_2$ has a direct band gap (E_g) of 4.74 eV, making it a semiconductor.[11] Moreover, a good approach to expand the uses of 2D materials is to build a heterostructure using two distinct layered materials.[24,25] In the heterostructure, 2D $Mg(OH)_2$ displayed distinctive structural and electrical properties.[26,27] Most recently, Suslu *et al.*[23] reported the effective separation of highly crystalline $Mg(OH)_2$ from 2D layered $Mg(OH)_2$. The unique optical and electronic characteristics of heterostructures that can be produced by combining other 2D materials with $Mg(OH)_2$ were also highlighted in this work.[28,29] By combining the benefits of its semiconductor structure, the van der Waals heterostructure (vdWH) can improve its optical and electrical capabilities in photocatalysis. Catalysis, electronics, and optoelectronics have all benefited from the unique optical, interfacial and electronic properties of vdWH.[30–32] Moreover, several $Mg(OH)_2$-based vdWHs have been investigated, such as $Mg(OH)_2$/AlN,[28] blue phosphorus/$Mg(OH)_2$[11] and $Mg(OH)_2$/WS_2.[29] The work functions, electronic band structure and spin–orbit coupling of different 2D materials may be used to create new 2D vdWH devices with a range of practical uses.[33]

Recent studies have demonstrated the potential of 2D materials and heterostructures for photocatalytic applications. For instance, Cui *et al.*[34] highlighted the importance of band-gap engineering in optimizing photocatalytic performance and explored the role of alloying in enhancing charge separation.[35] Building on these advancements, we propose the $B_2CSe/Mg(OH)_2$ vdWH as a novel device. Even though research on $Mg(OH)_2$-based heterostructures has advanced significantly, little is known about the potential stacking of B_2CSe and $Mg(OH)_2$ as well as its electronic and optical properties. It would be fascinating to do more research to determine if B_2CSe and $Mg(OH)_2$ may be stacked together and whether intriguing optical and electronic characteristics can be derived from such a heterostructure. Additionally, the hexagonal structures of B_2CSe and $Mg(OH)_2$ exhibit a small lattice mismatch. Thus, we conducted first principles simulations to examine the heterostructures created by B_2CSe and $Mg(OH)_2$ monolayers. The thermal and dynamic stability is considered once the structure of the heterostructure is determined. Then, the interfacial characteristics, including the potential drop, charge density difference and band alignment of the $B_2CSe/Mg(OH)_2$ vdWH, are checked. Type II band alignment, where the valence band maximum (VBM) and conduction band minimum (CBM) lie on opposing layers, may be produced *via* 2D semiconducting heterostructures. The distinct type II band alignment can efficiently separate photoexcited charge carriers into different heterostructure monolayers, which is advantageous for photocatalytic water splitting. This effectively reduces the recombination of electron–hole pairs, which leads to long photoexcited carrier lifetimes, ultrafast charge transfer and lower E_g.

II. Computation details

All computations are performed using the plane wave method based on density functional theory (DFT) implemented in the Quantum Espresso code.[36,37] In structural optimization, the exchange–correlation functional is treated by applying the Perdew–Burke–Ernzerhof (PBE) technique in conjunction with the generalized gradient approximation (GGA).[38] The atomic valence configurations of Mg, O, H, B, C and Se are $3s^2$, $2s^2\,2p^4$, $1s^1$, $2s^2\,2p^1$, $2s^2\,2p^2$ and $4s^2\,4p^4$, respectively. The plane wave cut-off energy of 50 Ry is appropriate to warrant the convergence of the total energy of the relaxed lattice vector and atomic positions. Furthermore, the *k*-point grid of energy convergence is set as $16 \times 16 \times 1$ for structural optimization and electronic property calculations with the Monkhorst–Pack technique.[39] During the optimization, the Hellmanne–Feynman force and energy converged to 1×10^{-3} Ry Bohr^{-1} and 1×10^{-6} Ry, respectively. These convergence criteria were consistently applied across all strain values to ensure the reliability and consistency of our results. This ensures that the atomic configurations are fully relaxed, and the system has a minimum energy. To accurately represent the long-range vdW interactions that are not present in the typical PBE function, the Grimme DFT-D3(BJ)[40,41] technique is used. A significant vacuum thickness of 30 Å is introduced along the *z*-axis to remove the contact between periodic images. The Heyd–Scuseria–Ernzerhof (HSE06) hybrid functional is used to simulate accurate electronic and optical properties since the PBE functional usually underestimates the E_g energy of 2D materials.[42] The fraction of the exact exchange parameter was set to $\alpha = 0.25$. Furthermore, *ab initio* molecular dynamics (AIMD) simulations and the computation of phonon spectra were used to evaluate the thermal and structural stability. The interfacial binding energy (E_b) of $B_2CSe/Mg(OH)_2$ can be accessed using the following formula to compare the stability of different stacking patterns:

$$E_b = (E_{B_2CSe/Mg(OH)_2} - E_{B_2CSe} - E_{Mg(OH)_2})/SA \qquad (1)$$

where, E_{B_2CSe} and $E_{Mg(OH)_2}$ are the energies of B_2CSe and $Mg(OH)_2$ monolayers, respectively, and $E_{B_2CSe/Mg(OH)_2}$ is the total energy of the $B_2CSe/Mg(OH)_2$ vdWH and SA is the $B_2CSe/Mg(OH)_2$ surface area. The formula above states that a heterostructure is stable if the E_b is negative and that the stability of the heterostructure is determined by the magnitude of its absolute value.[43] Thus, the more negative the E_b is, the more stable the structure is.

III. Results and discussion

Before exploring the $B_2CSe/Mg(OH)_2$ vdWH, we first performed high-precision optimization of the $Mg(OH)_2$ and B_2CSe

Table 1 Lattice constant (a = b), bandgap (E_g), interface binding energy (E_b), elastic constants (C_{ij}), the Poisson ratio (ν), Young's- (Y), shear- (G) and bulk- (B) moduli of $Mg(OH)_2$ and B_2CSe monolayers, and the stacking configurations of the $B_2CSe/Mg(OH)_2$ vdWH

Parameters	B_2CSe	$Mg(OH)_2$	Stacking I	Stacking II
$a = b$ (Å)	2.963	3.172	3.067	3.067
E_g (eV)	2.85	4.78	2.45	2.37
E_b (eV Å^{-2})	—	—	−12.039	−8.118
d (Å)	—	—	3.122	2.960
ΔV	—	—	8.06	8.35
$\|e\|$	—	—	0.0045	0.0003
d_{B-Se} (Å)	2.013	—	2.055	2.054
d_{B-C} (Å)	1.717	—	1.777	1.778
D_{Mg-O} (Å)	—	2.086	2.065	2.066
d_{O-H} (Å)	—	0.977	0.964	0.962
C_{11} (N m^{-1})	102.97	27.15	65.26	65.50
C_{12} (N m^{-1})	7.53	7.95	6.56	6.54
C_{66} (N m^{-1})	47.72	9.60	29.34	29.48
Y (N m^{-1})	102.42	24.83	64.60	64.85
ν	0.07	0.29	0.10	0.10
B (N m^{-1})	55.25	17.55	35.91	36.02
G (N m^{-1})	67.925	78.35	90.62	91.24

monolayers with the lattice parameters of 3.172 and 2.963 Å (Table 1), respectively, which agreed with earlier calculations (3.140 Å for $Mg(OH)_2$[30] and 2.970 Å for B_2CSe[44]).

The B–C/Se bond length is 1.717/2.013 Å, while the Mg–O and O–H bond lengths are 2.086 and 0.977 Å, respectively. B–C and B–Se bonds are connected by bonds of B–C with lengths of about 1.632 Å. The calculated bond lengths are in good agreement with earlier research.[44,45] Fig. 1(a) and (e) show the side and top views of the optimized structures of $Mg(OH)_2$ and B_2CSe monolayers. Next, a vdWH was created by vertically stacking the optimized $Mg(OH)_2$ monolayer over the optimized B_2CSe monolayer. An important consideration for evaluating the success of heterostructure development is lattice mismatch.[46] The lattice mismatch of the built $B_2CSe/Mg(OH)_2$ vdWH is 3.41%, which is sufficiently low to guarantee the system's stability.[47] Due to the hexagonal structures of $Mg(OH)_2$ and B_2CSe monolayers, both of which have significant flexibility, the constructed vdWH is stabilized when the lattice misfit is $<$5%,[48] which is within an acceptable region and can be achieved in experimental fabrication. Therefore, placing a unit cell of B_2CSe monolayer on top of a unit cell of $Mg(OH)_2$ monolayer is much more feasible in practical applications to generate the $B_2CSe/Mg(OH)_2$ vdWH.

The HSE06 hybrid functional was chosen for its improved accuracy in predicting electronic properties, particularly bandgaps, compared to standard generalized gradient approximation (GGA) functionals like PBE. PBE is known to underestimate bandgaps due to its inherent self-interaction error, while HSE06 mitigates this issue by incorporating a portion of the exact Hartree–Fock exchange (α = 0.25). This makes HSE06 more reliable for systems where accurate bandgap and band alignment

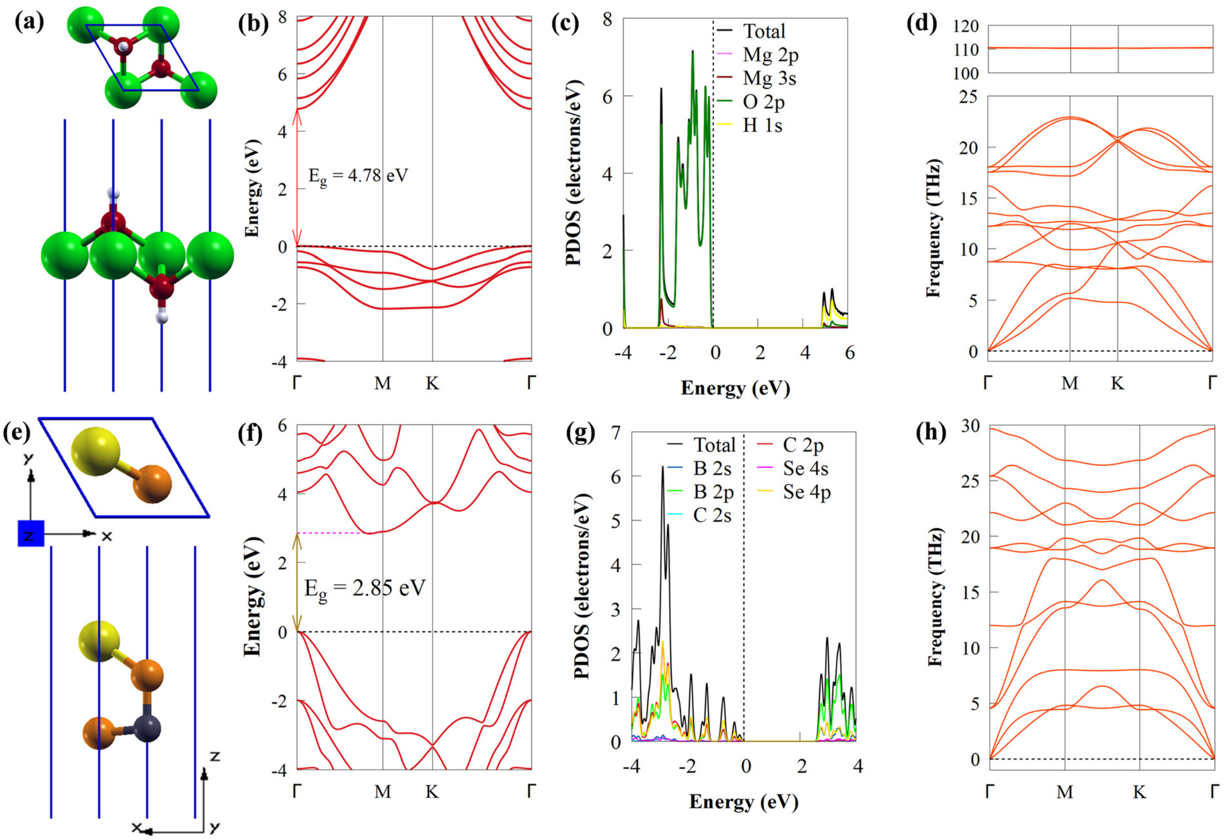

Fig. 1 Optimised structures of (a) $Mg(OH)_2$ and (e) B_2CSe; the red, green, white, grey, yellow and orange spheres signify O, Mg, H, C, Se and B atoms, respectively. The band structure of pristine (b) $Mg(OH)_2$ and (f) B_2CSe obtained by the HSE06 functional. The PDOS of pristine (c) $Mg(OH)_2$ and (g) B_2CSe. The phonon dispersion spectrum of pristine (d) $Mg(OH)_2$ and (h) B_2CSe.

predictions are critical, such as in vdWHs. The comparison shows that HSE06 provides bandgaps closer to experimental or high-level theoretical reference values, whereas PBE significantly underestimates them. This supports our choice of HSE06 for accurate electronic structure calculations (Fig. S1 and Table S1, ESI†). Fig. 1(b) and (f) depict the band structures of $Mg(OH)_2$ and B_2CSe monolayers, respectively. As a direct E_g semiconducting material, the 2D $Mg(OH)_2$ monolayer has both the VBM and CBM placed at the Γ symmetry point. The E_g of 4.78 eV aligns with previous findings.[23] Fig. 1(c) shows that the O 2p state is responsible for the VBM of the $Mg(OH)_2$ monolayer, while the H 1s state mostly regulates the CBM. For Janus B_2CSe, the CBM is situated at the M point and involves the p orbital of the B atom with contribution from the Se 4p and B 2s state character. In contrast, the VBM situated at the Γ symmetry point has the Se 4p orbital with contribution from C 2p and B 2p orbitals, showing an indirect E_g of 2.85 eV, consistent with earlier reports with E_g of 2.88 eV.[44]

To evaluate the stability, we looked at two different $B_2CSe/Mg(OH)_2$ vdWH configurations, as displayed in Fig. 2(a) and (b), in which the B_2CSe monolayer is moved while the $Mg(OH)_2$ monolayer is kept fixed. For the stacking I and II configurations, Se and B atoms in the B_2CSe monolayer are stacked on top of the H atom of $Mg(OH)_2$, respectively. The E_b for the two vdWH is all negative. The results demonstrate that the E_b per surface area of the $B_2CSe/Mg(OH)_2$ vdWH in the stacking I and II configurations, and the related equilibrium distances are −12.039 and −8.118 eV Å^{-2}, and 3.122 and 2.960 Å, respectively. The more negative E_b indicates that stacking I is thermodynamically stable, and subsequent discussion will be based on this configuration.

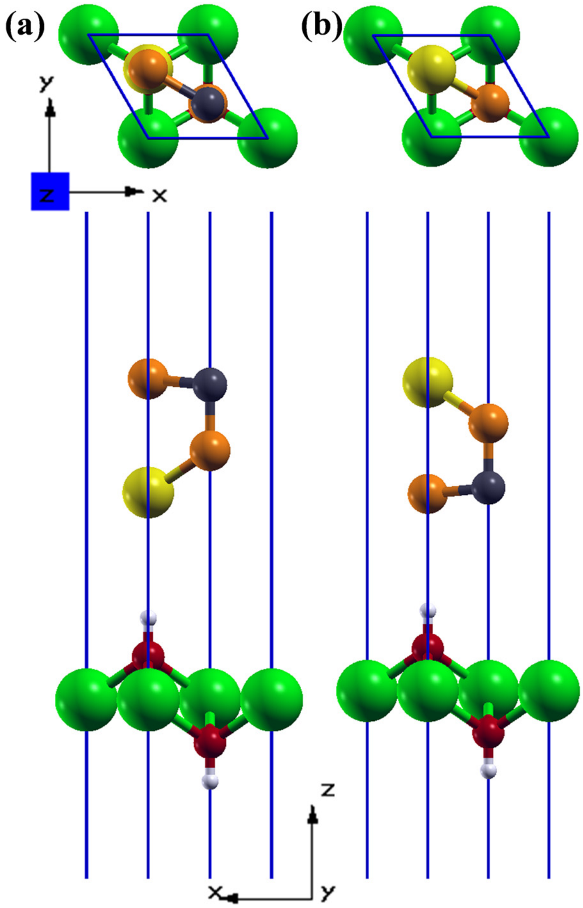

Fig. 2 Optimised structures of the two possible stackings of the $B_2CSe/Mg(OH)_2$ vdWH (a) stacking I and (b) II configurations of the $B_2CSe/Mg(OH)_2$ vdWH. The red, green, white, grey, yellow and orange spheres signify O, Mg, H, C, Se and B atoms, respectively.

Mechanical, thermodynamic, and kinetic stability are all important factors to consider. To verify the stability of the $B_2CSe/Mg(OH)_2$ vdWH, the 3 × 3 supercell (containing 81 atoms) was built and then heated at 300 K for 50 ps. The result shows that the heterostructures have no obvious structural changes after 50 ps at room temperature. Additionally, variations in temperature and total energy throughout the heating process are maintained in a small range, which proves that the $B_2CSe/Mg(OH)_2$ vdWH is thermally stable. The dynamic stability of the vdWH is considered using the phonon dispersion, as shown in Fig. 1(d), (h) and 3(b). The results demonstrate the dynamic stability by demonstrating the lack of negative frequency mode in the $B_2CSe/Mg(OH)_2$ vdWH.

It has been demonstrated that in practical applications, mechanical qualities are critical. The hexagonal system yielded four distinct elastic constants: C_{11}, C_{12}, C_{66} and C_{2D}. The in-plane elastic modulus (C_{2D}) positively correlates with the structure's strain resistance. The C_{2D} is expressed as:

$$C_{2D} = \frac{{C_{11}}^2 - {C_{12}}^2}{C_{11}} \tag{2}$$

The C_{11}, C_{12} and C_{66} of the $B_2CSe/Mg(OH)_2$ vdWH are significantly more than those of the $Mg(OH)_2$ and B_2CSe monolayers. Furthermore, the elastic constants satisfy the Born conditions in the following ways: $C_{11} > 0$; $C_{11} - C_{12} > 0$; and $C_{11} > |C_{12}|$.[49] These connections show that the $B_2CSe/Mg(OH)_2$ vdWH, and the isolated $Mg(OH)_2$ and B_2CSe monolayers are mechanically stable.[50] Fig. 3(c) and (d) show the angle-dependent $\nu(\theta)$ and $Y(\theta)$ polar plots. Young's modulus of the $Mg(OH)_2$ and B_2CSe monolayers and the $B_2CSe/Mg(OH)_2$ vdWH show anisotropy behaviour. The calculated Poisson ratio is within a reasonable range (0–0.5)[51] to favourably serve as an electrode material.[52] The C_{2D} values for B_2CSe, $Mg(OH)_2$ and the $B_2CSe/Mg(OH)_2$ vdWH are 102.42, 24.82, and 64.60, respectively. Compared to the $Mg(OH)_2$ monolayer, the strain resistance of $B_2CSe/Mg(OH)_2$ vdWH is higher.

A suitable band structure is crucial for semiconductor photocatalysts. The calculated band structure and PDOS of the $B_2CSe/Mg(OH)_2$ vdWH are given in Fig. 4. The CBM aligns with the high symmetry point of the B_2CSe monolayer close to M, whereas the VBM aligns with the high symmetry point Γ for the $Mg(OH)_2$ monolayer. This results in a type II band structure with an indirect E_g of 2.45 eV. A reduction in the bandgap makes it easier for electrons to be excited from the valence band to the conduction band. Increased overlap between the valence and conduction bands facilitate more efficient optical transitions leading to enhanced absorption in the visible range. These

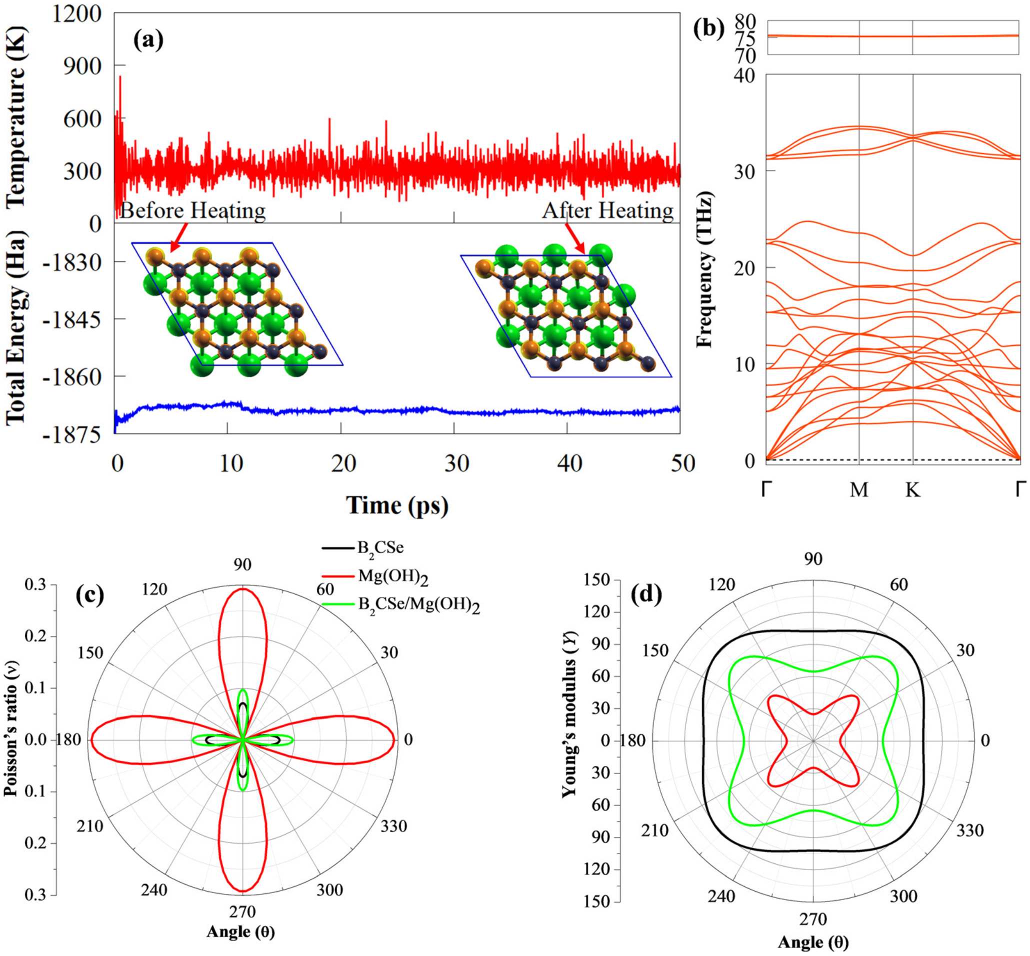

Fig. 3 (a) Temperature and total energy fluctuations of stacking I configuration of the $B_2CSe/Mg(OH)_2$ vdWH after annealing for 50 ps under 300 K during the AIMD simulation. The snapshot of the $B_2CSe/Mg(OH)_2$ vdWH after annealing for 50 ps is shown as an inset. (b) Phonon mode of the $B_2CSe/Mg(OH)_2$ vdWH. Angel-dependent (c) Poisson's ratio and (d) Young's modulus of B_2CSe, $Mg(OH)_2$ and the $B_2CSe/Mg(OH)_2$ vdWH.

E_g values are comparable to the indirect E_g of 2.15 (1.75) eV for the WS_2 $(MoS_2)/Mg(OH)_2$ vdWH, respectively,[45] indirect E_g of 2.21 eV for the BlueP/$Mg(OH)_2$ vdWH,[11] 2.31 eV for the h-AlN/$Mg(OH)_2$ vdWH[28] and the direct E_g of 2.23 (1.99) eV for the WSSe (MoSSe)/$Mg(OH)_2$ vdWH, respectively,[53] but larger than the direct E_g of 1.40 eV for the $Ca(OH)_2/\alpha$-$MoTe_2$ vdWH,[54] 1.45 eV for the GaS/$Ca(OH)_2$ vdWH[55] and 0.72 eV for the Te/$Ca(OH)_2$[56] vdWH. Type II band alignment enables the spontaneous separation of free electron–hole pairs, resulting in very effective solar energy conversion devices. Our findings indicate that the vdWH bandgap is reduced compared to the $Mg(OH)_2$ (4.78 eV). The $B_2CSe/Mg(OH)_2$ vdWH have E_g that fulfil the minimum E_g criteria (1.23 eV) for photocatalytic water splitting processes. The PDOS analysis in Fig. 4(b) shows that the O 2p orbital contributes to the VBM of the $B_2CSe/Mg(OH)_2$ vdWH, whereas the B 2p orbital contributes to the CBM along with the B 2s and Se 4p orbitals. The substantial charge transfer from O to B suggests the formation of strong covalent bonds between these atoms. This redistribution likely leads to new electronic states near the Fermi level, which can influence the material's electronic and optical behaviour. The PDOS shows an increase in states near the CBM or VBM, which indicates that charge redistribution has created additional electronic states that can participate in optical transitions.

To further comprehend the charge transfer between the B_2CSe and $Mg(OH)_2$ interface, the plane average charge density ($\Delta\rho$) and charge density difference (CDD) were used. As displayed in Fig. 5(a), red denotes electron accumulation and blue denotes electron depletion. $\Delta\rho$ is positive near the B_2CSe monolayer while negative near the $Mg(OH)_2$ monolayer (Fig. 5(b)). This implies that the $Mg(OH)_2$ monolayer acts as an electron donor while the B_2CSe monolayer receives the electrons. This means that electrons are transferred from the $Mg(OH)_2$ monolayer to the B_2CSe monolayer. In the interface region, the produced dipole moment causes a built-in electric field pointing towards the B_2CSe monolayer in a direction perpendicular to the surface. The electrons (holes) are moving from the $Mg(OH)_2$ (B_2CSe) monolayer to the B_2CSe ($Mg(OH)_2$) monolayer because of the built-in electric field (Fig. 5(c)). The Bader charge analysis[57] results in Table 2 show that B_2CSe gains 0.0045 $|e|$. The C/Se atoms lose an average of 2.7580/0.8737 $|e|$, while each B atom gains an average of 1.8181 $|e|$. The $Mg(OH)_2$ loses 0.0045 $|e|$. The

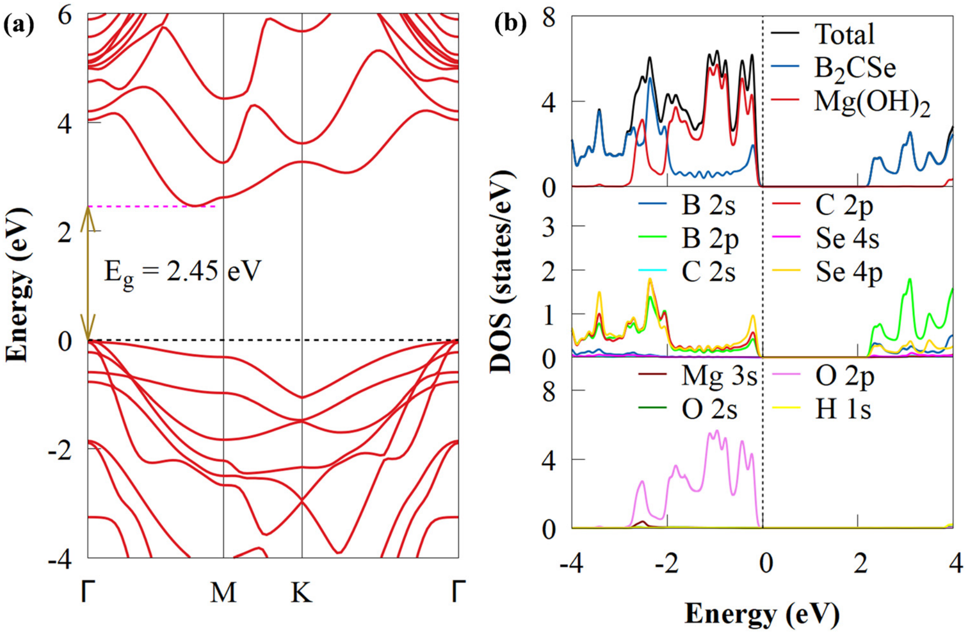

Fig. 4 (a) Band structures and the corresponding (b) PDOS of the $B_2CSe/Mg(OH)_2$ vdWH.

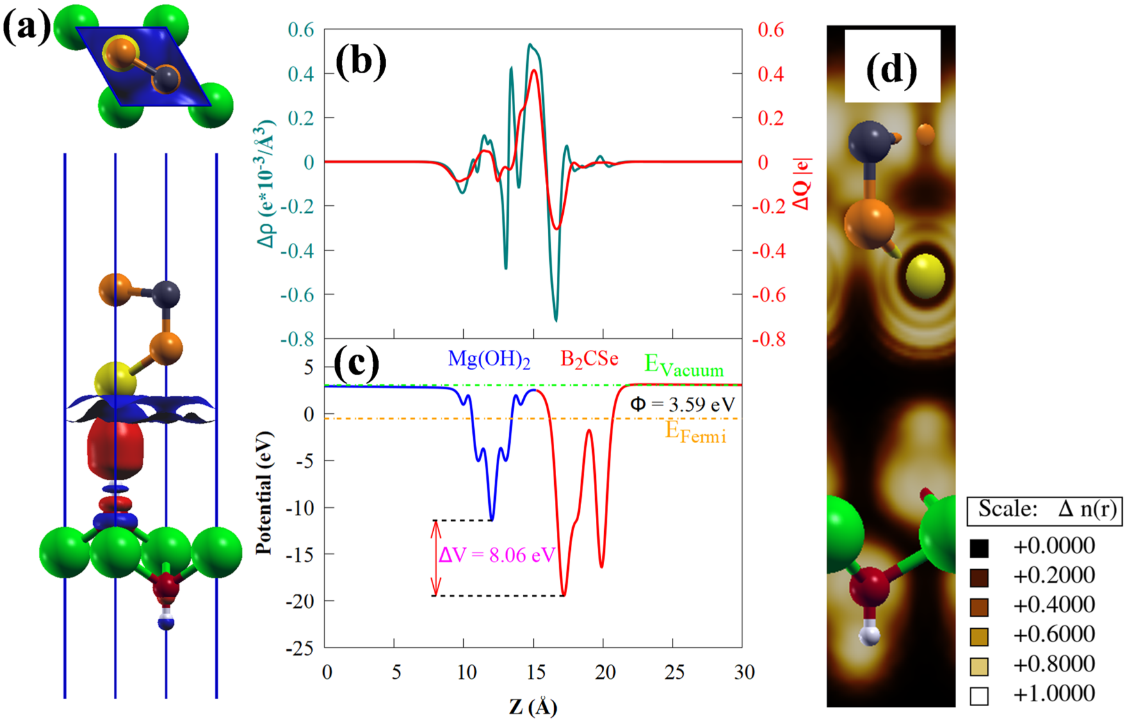

Fig. 5 (a) Three-dimensional charge density difference of the $B_2CSe/Mg(OH)_2$ vdWH. The depletion and accumulation of charges are denoted by blue and red isosurfaces, respectively; the isovalue is set as 0.00005 Ry Bohr^{-3}. The plane average charge density (b) and (c) electrostatic potential of the $B_2CSe/Mg(OH)_2$ vdWH along the *z*-axis. (d) Electron localization function of the $B_2CSe/Mg(OH)_2$ vdWH.

Mg/H atoms gain an average of 1.7073/0.9999 $|e|$, while the O atom loses an average of 1.8558 $|e|$. The difference in charge transfer magnitude may arise from differences in the electronic structure, band alignment, and interfacial bonding between the two systems. The strength of the built-in electric field is highly sensitive to the spatial distribution of the transferred charges. A small amount of charge transfer concentrated at the interface can still generate a significant electric field due to the sharp

Table 2 Work function (Φ) and Bader charge analysis of $Mg(OH)_2$ and B_2CSe. The negative charge value indicates electron loss, while the positive charge value implies electron gain

Monolayers	Φ (eV)	Layer/charge $\|e\|$	Atom/average charge $\|e\|$ per atom					
B_2CSe	4.63	+0.0045	B	C	Se	Mg	O	H
$Mg(OH)_2$	4.34	−0.0045	+1.8181	−2.7580	−0.8737	+1.7073	−1.8558	+0.9999

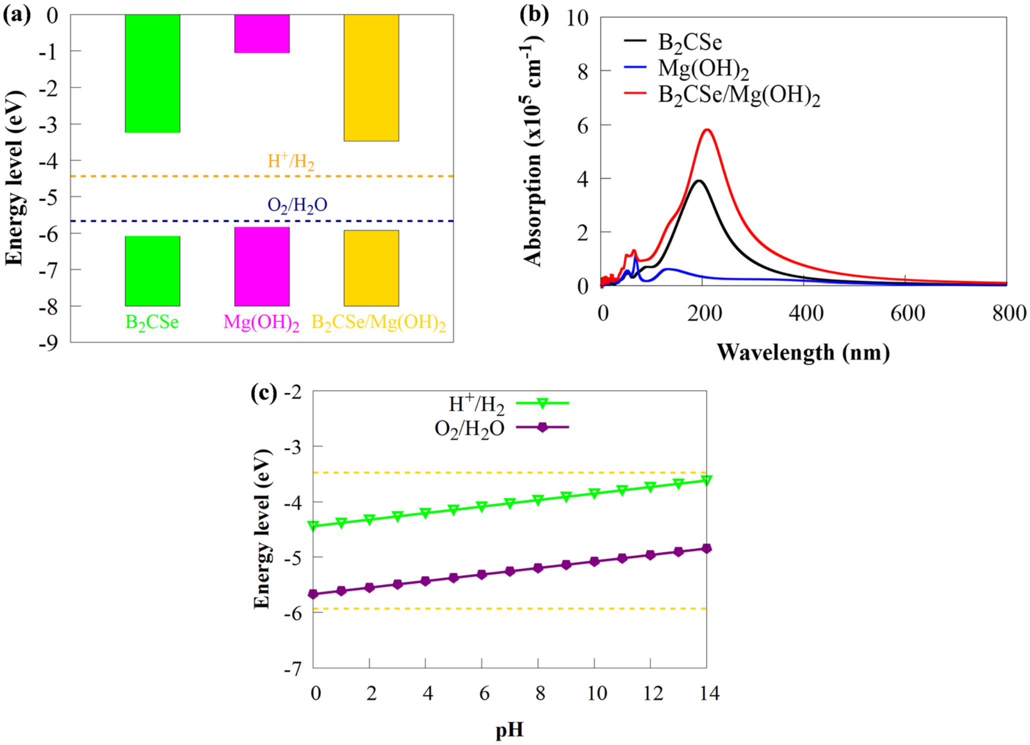

Fig. 6 (a) Band edge positions of the $Mg(OH)_2$, B_2CSe and $B_2CSe/Mg(OH)_2$ vdWH with reference to water redox reaction potentials at pH = 0. (b) Optical properties of $Mg(OH)_2$, B_2CSe and $B_2CSe/Mg(OH)_2$ vdWH. (c) Band edge positions of the $B_2CSe/Mg(OH)_2$ vdWH at pH = 0–14.

potential gradient. Even a small charge transfer can form a built-in electric field, as the spatial separation of charges across the interface creates a dipole moment. The strength of the electric field depends not only on the magnitude of the charge transfer but also on the distance over which the charges are separated. In vdWHs, the interlayer distance is typically larger than in covalently bonded systems, which can amplify the effect of even a small charge transfer in creating a measurable electric field. The weak charge transfer indicates that the interaction between $Mg(OH)_2$ and B_2CSe is predominantly governed by vdW forces rather than strong covalent or ionic bonding.

Understanding the charge transfer at the $B_2CSe/Mg(OH)_2$ vdWH interface can be achieved by analysing the work function (Φ) for the B_2CSe and $Mg(OH)_2$ monolayers. The Φ values of B_2CSe and $Mg(OH)_2$ monolayers and the $B_2CSe/Mg(OH)_2$ vdWH are 4.63, 4.34 and 3.59 eV, respectively. The work function results agree with those of earlier studies (4.248 eV for $Mg(OH)_2$[58]). The higher Φ of the B_2CSe monolayer allows charges to transfer from $Mg(OH)_2$ to B_2CSe during heterostructure development until they reach the same Fermi level. The charge redistribution around the $B_2CSe/Mg(OH)_2$ vdWH interface is caused by the difference in Φ. This demonstrates that an electric field exists at the interface. The potential drop (ΔV) at the interface is 8.06 eV. It is commonly recognised that a high electric field coincides with a large ΔV. Consequently, the interface region of the vdWH experiences a high electric field due to the significant electrostatic potential difference. The interfacial dipole moment is often a direct consequence of charge transfer. When electrons move from one material to another, a charge imbalance is created, forming a dipole moment. The interfacial dipole moment per unit area is given by:

$$\mu_{\text{int}} = \varepsilon_0 \int_{z_1}^{z_2} (\phi(z) - \phi_\infty)\mathrm{d}z \qquad (3)$$

where ε_0 is the permittivity of free space (8.854×10^{-12} F m^{-1}), $\phi(z)$ is the electrostatic potential profile, ϕ_∞ is the reference potential (usually taken in the bulk region), and the z_1 and z_2 define the interfacial region. The greater the charge transfer, the larger the dipole moment. The computed interfacial dipole moments of -1.07×10^{-10} and -1.05×10^{-10} C m for stacking I and II highlight significant charge transfer and electronic redistribution

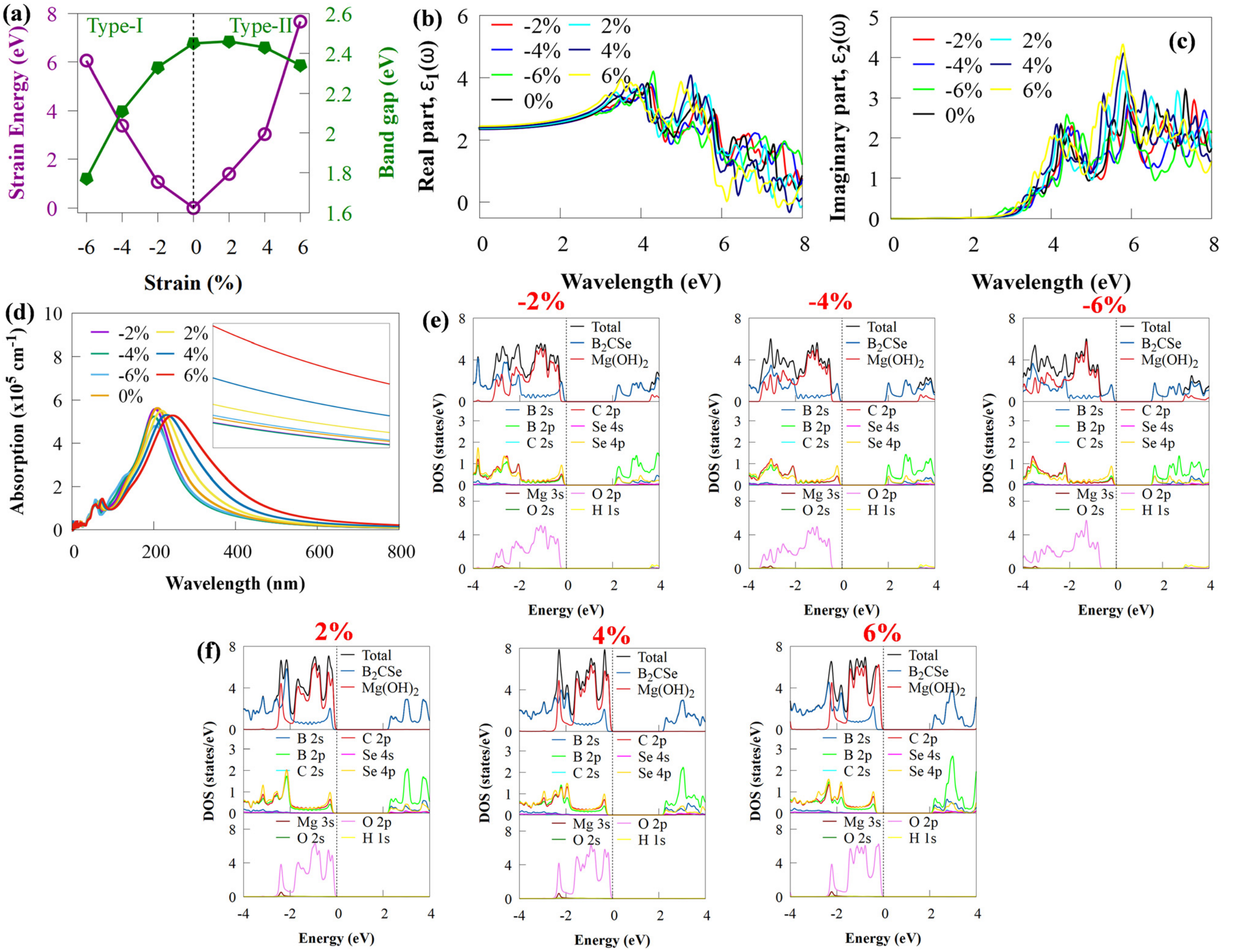

Fig. 7 (a) Strain energy and evolution of the bandgap, (b) real part of dielectric function, (c) imaginary part of dielectric function and (d) evolution of light absorption coefficients of the $B_2CSe/Mg(OH)_2$ vdWH with an applied biaxial strain. PDOS of the $B_2CSe/Mg(OH)_2$ vdWH under (e) compressive and (f) tensile biaxial strains.

at the interface. However, a slight difference may arise from variations in atomic arrangement at the interface. These values are consistent with those reported in similar systems (graphene/MoS_2,[59] and metal–organic interfaces[60]). When $Mg(OH)_2$ is used as an electrode, the high ΔV indicates a strong electric field at the interface, potentially significantly affecting electron transfer.

The band edge positions for redox reactions are essential for an efficient photocatalyst. The B_2CSe, $Mg(OH)_2$ and $B_2CSe/Mg(OH)_2$ vdWH have conduction band edges of −3.694, −1.059 and −3.469 eV, respectively. B_2CSe, $Mg(OH)_2$ and $B_2CSe/Mg(OH)_2$ are estimated to have valence band edge energies of −6.546, −5.839, and −5.929 eV, respectively. The photoactivity is largely influenced by the valence band offsets (VBOs) and the conduction band offsets (CBOs), which are the relative positions of the VBM and the CBM.[61] The VBO/CBO is 0.71/2.63 eV. As seen in Fig. 6(a), the redox capability can be evaluated by positioning the CBM and VBM with reference to the water redox potentials.

The $Mg(OH)_2$ monolayer has feasible band locations for water splitting; however, their VBM overpotential may not be adequate for O_2 generation. The large band gap of the monolayer (>2.20 eV) prevents it from absorbing a sizable part of the solar energy spectrum, which lowers the conversion efficiency. Nevertheless, the B_2CSe monolayer's VBM is less favourable for overall water splitting since it is less positive than the H_2O/O_2 potential. The overpotential of the $B_2CSe/Mg(OH)_2$ vdWH may be sufficient to generate adequate H_2 and O_2, and it has appropriate CBM and VBM positions for the reduction and oxidation potentials. Since pH influences the redox potential of water, the possibility of water splitting at pH values 0 to 14 is considered in this work. The CBM and VBM of the $B_2CSe/Mg(OH)_2$ vdWH at pH = 0 to 14 are always greater than the H^+/H_2 and H_2O/O_2 potentials of water. This means that the $B_2CSe/Mg(OH)_2$ vdWH can always split water with a pH between 0 and 14. Notably, the band edge position is largely unaffected by pH, signifying that the $B_2CSe/Mg(OH)_2$ vdWH photocatalyst can be successfully used in alkaline and acidic conditions.

Strain is a useful technique to modulate the electronic structure of 2D materials, producing more intriguing and advantageous properties.[62] Therefore, the $B_2CSe/Mg(OH)_2$ vdWH was

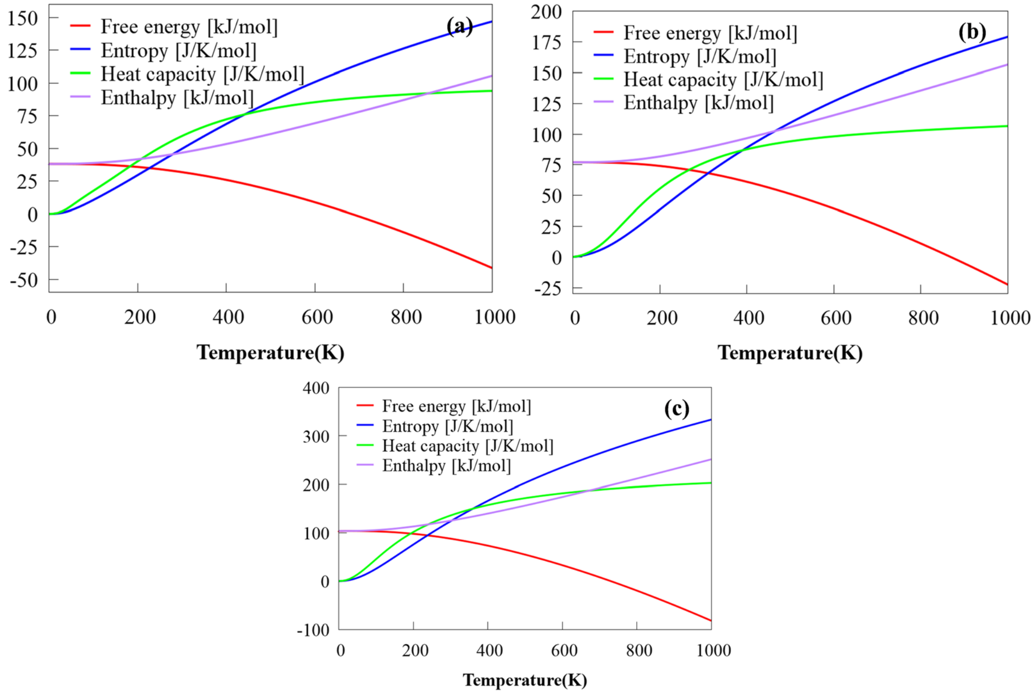

Fig. 8 Free energy, entropy, heat capacity and enthalpy against temperature for (a) B_2CSe, (b) $Mg(OH)_2$ and (c) $B_2CSe/Mg(OH)_2$ vdWH.

subjected to a biaxial strain (−6% to +6%). The lattice constant was changed to simulate the $B_2CSe/Mg(OH)_2$ vdWH strain. The biaxial strain (ε) that is imposed is evaluated as:

$$\varepsilon = \frac{l - l_0}{l_0} \times 100\% \quad (4)$$

where the strained and unstrained lattice constants are denoted by l and l_0, respectively. Furthermore, the following is the expression for the strain energy (E_s):

$$E_s = E_{\text{strain}} - E_{\text{unstrain}} \quad (5)$$

where E_{unstrain} and E_{strain} signify the total energy of the $B_2CSe/Mg(OH)_2$ vdWH before and after biaxial strain is applied, respectively. Fig. 7(a) illustrates how the band gap and strain energy change with biaxial strain for the $B_2CSe/Mg(OH)_2$ vdWH.

Positive values represent tensile strain, whereas negative values represent compressive strain. The parabolic pattern in the strain energy change indicates that the $B_2CSe/Mg(OH)_2$ vdWH are in the elastic deformation range. To further comprehend the modulation mechanism of the biaxial strain effect on the electronic characteristics of the $B_2CSe/Mg(OH)_2$ vdWH, Fig. S4 (ESI†) shows the projected band structures. The corresponding PDOS under various biaxial strains is shown in Fig. 7(e) and (f). The band gap values decrease as the tensile strain increases from 0% to +6%. When biaxial tensile strain is applied from 0% to +6%, the $B_2CSe/Mg(OH)_2$ vdWH band structure maintains an indirect bandgap and type II band alignment. Nevertheless, the $B_2CSe/Mg(OH)_2$ vdWH band gap decreases when the compressive biaxial strain increases. Furthermore, the VBM of $B_2CSe/Mg(OH)_2$ vdWH changes from $Mg(OH)_2$ to B_2CSe because of the notable decrease in the VBM of $Mg(OH)_2$ at the Γ point. These changes result in a type II to type I transition by decreasing the band gap. The CBM and VBM of the $B_2CSe/Mg(OH)_2$ vdWH are then dominated by B_2CSe. The strain-induced band alignment transition in the $B_2CSe/Mg(OH)_2$ vdWH is consistent with observations in other systems.[63] However, our system demonstrates a more pronounced tunability, making it highly adaptable for strain-modulated photocatalytic applications.[34,64]

A photocatalyst performance is strongly influenced by how well it absorbs light. This implies that effective photocatalysts should be highly capable of absorbing light, particularly in the visible region. As seen in Fig. 6(b), the absorption capacities of $Mg(OH)_2$ and B_2CSe monolayers and $B_2CSe/Mg(OH)_2$ vdWH are examined. The B_2CSe monolayer exhibits a certain absorption ability in the visible light range of 380–500 nm. However, the absorption of the $Mg(OH)_2$ monolayer is primarily observed in the ultraviolet region, with limited absorption in the visible spectra. Thus, the $Mg(OH)_2$ monolayer has a higher UV absorption coefficient and lower visible light absorption than the B_2CSe monolayer. As a result of the overlapping electronic states engendered by interlayer coupling effects, the $B_2CSe/Mg(OH)_2$ vdWH with a narrower bandgap exhibits outstanding optical absorption in the visible wavelength region (about 300–600 nm) compared with the B_2CSe and $Mg(OH)_2$ monolayers. The $B_2CSe/Mg(OH)_2$ vdWH exhibits excellent absorption in the UV and visible range and significantly enhances the absorption coefficient.

The absorption spectra of the $B_2CSe/Mg(OH)_2$ vdWH at various strains are shown in Fig. 7(d). When tensile strain rises from 0% to +6%, the absorption intensity in the visible light spectrum gradually improves, although it is higher under compressive strain than without strain. In particular, the absorption spectra of $B_2CSe/Mg(OH)_2$ vdWH are observed to be red-shifted when the tensile strains of 0% to 6% are applied compared to compressive strain. As the tensile strain increases, the bandgap gradually decreases, causing the absorption peak to move to a broader wavelength. The hybridization between the electronic states of the B_2CSe and $Mg(OH)_2$ monolayers causes the visible light absorption edge under tensile strain by enabling the excitation of the electrons between them.

The computed free energy, enthalpy and entropy against temperature are displayed in Fig. 8. Entropy and enthalpy rise with temperature because of temperature variations. As the temperature rises, the free energy falls since the Gibbs free energy would drop with increasing temperature as it equals the enthalpy minus the product of entropy and temperature. Compared to B_2CSe and $Mg(OH)_2$ monolayers, the enthalpy and free energy of the $B_2CSe/Mg(OH)_2$ vdWH noticeably increases at higher temperatures.

Moreover, a crucial parameter for evaluating the photoactivity of the $B_2CSe/Mg(OH)_2$ vdWH is the solar-to-hydrogen (STH) efficiency (η_{STH}). Previous research[65] indicates that η_{STH} can be calculated as:

$$\eta_{STH} = \eta_{abs} \times \eta_{cu}, \tag{6}$$

where η_{abs} and η_{cu} are the efficiency of sunlight absorption and carrier utilization, respectively. The formulae of these two quantities are:

$$\eta_{abs} = \frac{\int_{E_g}^{\infty} P(\hbar\omega)d(\hbar\omega)}{\int_{0}^{\infty} P(\hbar\omega)d(\hbar\omega)} \tag{7}$$

$$\eta_{cu} = \frac{\Delta G \int_{E}^{\infty} \frac{P(\hbar\omega)}{\hbar\omega} \mathrm{d}(\hbar\omega)}{\int_{E_g}^{\infty} P(\hbar\omega)\mathrm{d}(\hbar\omega)} \tag{8}$$

where $P(\hbar\omega)$ denotes the AM1.5G solar flux at a photon energy of $\hbar\omega$, ΔG is the decomposition potential difference of water at pH = 0 (ΔG = 1.23 eV). The AM1.5G spectrum is the standard reference for solar energy conversion studies, as it represents the solar irradiance under specific atmospheric conditions (air mass 1.5) with a total integrated power of 1000 W m^{-2}. The integration is performed over the AM1.5G solar spectrum range of 280–4000 nm. This range encompasses over 99% of the solar energy available on the Earth's surface, making it the most relevant range for calculating STH efficiency. The overpotentials for HER ($\chi(H_2)$) and OER ($\chi(O_2)$) and E_g at pH 0 are used to determine the minimum photon energy (E), as follows:

$$E = \begin{cases} E_g(\chi(H_2) \geq 0.2, \chi(O_2) \geq 0.6) \\ E_g + 0.2 - \chi(H_2), (\chi(H_2) < 0.2, \chi(O_2) \geq 0.6) \\ E_g + 0.6 - \chi(O_2), (\chi(H_2) \geq 0.2, \chi(O_2) < 0.6) \\ E_g + 0.8 - \chi(H_2) - \chi(O_2), ((\chi(H_2) < 0.2, \chi(O_2) < 0.6) \end{cases} \tag{11}$$

At pH 0, we obtain the OER overpotential = 5.929 − 5.67 = 0.259 eV and the HER overpotential = 4.44 − 3.469 = 0.971 eV. We obtain $E = E_g + 0.6 - \chi O_2 = 2.45 + 0.6 - 0.259 = 2.791$ eV from eqn (11). Using eqn (7) and (8) and the lower limits of integration E_g = 2.45 eV and E = 2.791 eV, the η_{STH} of the $B_2CSe/Mg(OH)_2$ vdWH is then calculated using eqn (11). It is believed that when the STH efficiency is at least 10% or higher, photocatalytic water splitting can produce hydrogen.[66] The η_{STH} for the $B_2CSe/Mg(OH)_2$ vdWH is 34.58%. The η_{STH} is greater than that of the other heterostructure photocatalysts, including GaN/InS (26.33%),[67] $PtS_2/g\text{-}C_3N_4$ (31.64%),[68] $g\text{-}C_6N_6/InP$ (27.32%),[69] Zr_2CO_2/WSe_2 (15.57%),[70] GeS/GeSe (31.21%),[71] and SeGe/SnS (26.45%).[72] The $B_2CSe/Mg(OH)_2$ vdWH shows exceptional photocatalytic performance, with a η_{STH} of 34.58%, outperforming many state-of-the-art systems, as highlighted in Cui *et al.*[73] This improvement is attributed to the optimized electronic properties, enhanced charge separation, and reduced recombination rates in the $B_2CSe/Mg(OH)_2$ vdWH. The $\eta_{STH}$of the $B_2CSe/Mg(OH)_2$ vdWH exceeds the industry benchmark of 10%, making it a promising H_2 producing photocatalyst. The results show that the $B_2CSe/Mg(OH)_2$ vdWH has improved photocatalytic performance across the solar spectrum.

IV. Conclusions

First-principle simulations with vdW corrections were explored systematically to study the geometry, optical and electronic properties of vdWH based on $Mg(OH)_2$ and Janus B_2CSe monolayers. $B_2CSe/Mg(OH)_2$ with mechanical, dynamical and thermal stability were created using vdW interactions. The negative E_b indicates the thermodynamic stability of $B_2CSe/Mg(OH)_2$ vdWH. The $B_2CSe/Mg(OH)_2$ vdWH had a semiconductor property, with an indirect E_g of 2.45 eV and a type II band structure, indicating they it is a good candidate for solar devices. The $B_2CSe/Mg(OH)_2$ vdWH has higher visible light absorption coefficients than the isolated monolayers. The η_{STH} reaches up to 34.58%, which benefits the harvest and utilization of solar energy. Charge analysis demonstrated that the $Mg(OH)_2$ monolayer donated 0.0045 $|e|$ to the B_2CSe monolayer. The comparatively substantial built-in field between B_2CSe and $Mg(OH)_2$ indicates a highly promising application in solar devices, which can efficiently lower the recombination of charge carriers. Compressive biaxial strain can tune the bandgap and band alignment with a transition from type II to type I. A tensile biaxial strain of +2% to +6% maintained the type II band alignment. The band edge locations at pH 0 to 14 show that the $B_2CSe/Mg(OH)_2$ vdWH is a promising water splitting photocatalyst. The splitting occurs spontaneously without any external voltage. This work offers theoretical support for designing a new potential 2D heterostructure for next generation solar devices.

Author contributions

Francis Opoku: conceptualization, data curation, formal analysis, investigation, methodology, and writing – original draft preparation. Eric Selorm Agorku, Samuel Osei-Bonsu Oppong, Edward

Ebow Kwaansa-Ansah, Noah Kyame Asare-Donkora, and Penny Poomani Govender: conceptualization, resources, methodology, formal analysis, and writing – review and editing. All authors reviewed the manuscript.

Data availability

The data supporting the findings of this study are included within the article.

Conflicts of interest

The authors declare that they have no known competing financial interests or personal relationships that could have appeared to influence the work reported in this paper.

Acknowledgements

We acknowledge the computational support provided by the Centre for High Performance Computing (CHPC), Cape Town.

References

1 Z. Pan, M. Zhao, H. Zhuzhang, G. Zhang, M. Anpo and X. Wang, *ACS Catal.*, 2021, **11**, 13463–13471.
2 F. Dawood, M. Anda and G. Shafiullah, *Int. J. Hydrogen Energy*, 2020, **45**, 3847–3869.
3 A. Martin, M.-F. Agnoletti and E. Brangier, *Int. J. Hydrogen Energy*, 2020, **45**, 11889–11900.
4 J. Chen, G. Qian, H. Zhang, S. Feng, Y. Mo, L. Luo and S. Yin, *Adv. Funct. Mater.*, 2022, **32**, 2107597.
5 P. Ganguly, M. Harb, Z. Cao, L. Cavallo, A. Breen, S. Dervin, D. D. Dionysiou and S. C. Pillai, *ACS Energy Lett.*, 2019, **4**, 1687–1709.
6 D. Gao, J. Xu, L. Wang, B. Zhu, H. Yu and J. Yu, *Adv. Mater.*, 2022, **34**, 2108475.
7 Q. Wang and K. Domen, *Chem. Rev.*, 2019, **120**, 919–985.
8 F. Opoku, O. Akoto, E. E. Kwaansa-Ansah, N. K. Asare-Donkor and A. A. Adimado, *Chem. Phys. Impact*, 2023, **6**, 100236.
9 K. Chang, Z. Mei, T. Wang, Q. Kang, S. Ouyang and J. Ye, *ACS Nano*, 2014, **8**, 7078–7087.
10 F. A. Frame and F. E. Osterloh, *J. Phys. Chem. C*, 2010, **114**, 10628–10633.
11 B.-J. Wang, X.-H. Li, X.-L. Cai, W.-Y. Yu, L.-W. Zhang, R.-Q. Zhao and S.-H. Ke, *J. Phys. Chem. C*, 2018, **122**, 7075–7080.
12 G. Swain, S. Sultana and K. Parida, *ACS Sustainable Chem. Eng.*, 2020, **8**, 4848–4862.
13 B.-J. Wang, X.-H. Li, R. Zhao, X.-L. Cai, W.-Y. Yu, W.-B. Li, Z.-S. Liu, L.-W. Zhang and S.-H. Ke, *J. Mater. Chem. A*, 2018, **6**, 8923–8929.
14 E. Koranteng-Mantey, C. Kessie, E. Selorm Agorku, E. E. Kwaansa-Ansah, S. Osei-Bonsu Oppong and F. Opoku, *ChemPhysChem*, 2024, **25**, e202300947.
15 M. Haruna, F. Eshun, C. K. Bandoh, E. S. Agorku, O. Francis, N. K. Asare–Donkor and A. A. Adimado, *Sustain. Chem. Environ.*, 2024, **5**, 100069.
16 A. K. Geim and K. S. Novoselov, *Nat. Mater.*, 2007, **6**, 183–191.
17 K. Ren, M. Sun, Y. Luo, S. Wang, J. Yu and W. Tang, *Appl. Surf. Sci.*, 2019, **476**, 70–75.
18 Y. Cai, J. Lan, G. Zhang and Y.-W. Zhang, *Phys. Rev. B: Condens. Matter Mater. Phys.*, 2014, **89**, 035438.
19 Y. Li, Q. Cui, F. Ceballos, S. D. Lane, Z. Qi and H. Zhao, *Nano Lett.*, 2017, **17**, 6661–6666.
20 M. Sun and U. Schwingenschlögl, *J. Phys. Chem. C*, 2021, **125**, 4133–4138.
21 S. Kumaravel, K. Karthick, S. Sam Sankar, A. Karmakar, R. Madhu, K. Bera and S. Kundu, *ChemElectroChem*, 2021, **8**, 4638–4685.
22 F. Opoku, A. Aniagyei, O. Akoto, E. E. Kwaansa-Ansah, N. K. Asare-Donkor and A. A. Adimado, *Next Mater.*, 2023, **1**, 100042.
23 A. Suslu, K. Wu, H. Sahin, B. Chen, S. Yang, H. Cai, T. Aoki, S. Horzum, J. Kang, F. M. Peeters and S. Tongay, *Sci. Rep.*, 2016, **6**, 20525.
24 K. Ren, R. Zheng, P. Xu, D. Cheng, W. Huo, J. Yu, Z. Zhang and Q. Sun, *Nanomater.*, 2021, **11**, 2236.
25 F. Opoku, O. Akoto, E. E. Kwaansa-Ansah, N. K. Asare-Donkor and A. A. Adimado, *Materials Advances*, 2023, **4**, 1949–1963.
26 K. Ren, J. Yu and W. Tang, *Phys. Lett. A*, 2019, **383**, 125916.
27 K. Ren, J. Yu and W. Tang, *J. Appl. Phys.*, 2019, **126**, 065701.
28 C. Bacaksiz, A. Dominguez, A. Rubio, R. T. Senger and H. Sahin, *Phys. Rev. B*, 2017, **95**, 075423.
29 M. Yagmurcukardes, E. Torun, R. T. Senger, F. M. Peeters and H. Sahin, *Phys. Rev. B*, 2016, **94**, 195403.
30 J. Lou, K. Ren, Z. Huang, W. Huo, Z. Zhu and J. Yu, *RSC Adv.*, 2021, **11**, 29576–29584.
31 F. Opoku, S. Osei-Bonsu Oppong, A. Aniagyei, O. Akoto and A. A. Adimado, *RSC Adv.*, 2022, **12**, 7391–7402.
32 F. Opoku, A. Aniagyei, O. Akoto, E. E. Kwaansa-Ansah, N. K. Asare-Donkor and A. A. Adimado, *Mater. Today Adv.*, 2022, **3**, 4629–4640.
33 S. Yang, C. Wang, C. Ataca, Y. Li, H. Chen, H. Cai, A. Suslu, J. C. Grossman, C. Jiang and Q. Liu, *ACS Appl. Mater. Interfaces*, 2016, **8**, 2533–2539.
34 Z. Cui, N. Liu, Y. Zhang and M. Wang, *Opt. Commun.*, 2024, **570**, 130874.
35 X. Gao, Z. Cui and P. Wu, *JAllC*, 2025, **1017**, 179127.
36 P. Giannozzi, S. Baroni, N. Bonini, M. Calandra, R. Car, C. Cavazzoni, D. Ceresoli, G. L. Chiarotti, M. Cococcioni, I. Dabo, A. Dal Corso, S. de Gironcoli, S. Fabris, G. Fratesi, R. Gebauer, U. Gerstmann, C. Gougoussis, A. Kokalj, M. Lazzeri, L. Martin-Samos, N. Marzari, F. Mauri, R. Mazzarello, S. Paolini, A. Pasquarello, L. Paulatto, C. Sbraccia, S. Scandolo, G. Sclauzero, A. P. Seitsonen, A. Smogunov, P. Umari and R. M. Wentzcovitch, *J. Phys.: Condens. Matter*, 2009, **21**, 395502.
37 P. Giannozzi, O. Baseggio, P. Bonfà, D. Brunato, R. Car, I. Carnimeo, C. Cavazzoni, S. d Gironcoli, P. Delugas,

F. F. Ruffino, A. Ferretti, N. Marzari, I. Timrov, A. Urru and S. Baroni, *J. Chem. Phys.*, 2020, **152**, 154105.
38 J. P. Perdew, K. Burke and M. Ernzerhof, *Phys. Rev. Lett.*, 1996, **77**, 3865–3868.
39 H. J. Monkhorst and J. D. Pack, *Phys. Rev. B*, 1976, **13**, 5188–5192.
40 S. Grimme, J. Antony, S. Ehrlich and H. Krieg, *J. Chem. Phys.*, 2010, **132**, 154104.
41 S. Grimme, S. Ehrlich and L. Goerigk, *J. Comput. Chem.*, 2011, **32**, 1456–1465.
42 J. Heyd, G. E. Scuseria and M. Ernzerhof, *J. Chem. Phys.*, 2003, **118**, 8207–8215.
43 Z.-B. Qiang, Y. Zhang, J.-X. Ding, K.-X. Xie, H. Nouguiza, H.-X. Chen, L. Duan, J.-B. Fan and L. Ni, *Int. J. Hydrogen Energy*, 2024, **51**, 809–821.
44 M. Ashhadi, *Indian J. Phys.*, 2024, **98**, 1699–1706.
45 Y. Luo, S. Wang, K. Ren, J.-P. Chou, J. Yu, Z. Sun and M. Sun, *Phys. Chem. Chem. Phys.*, 2019, **21**, 1791–1796.
46 Q. Zhang, P. Chen, Q. Liu, P. Sun, Y. Yi, J. Lei and T. Song, *Mater. Sci. Semicond. Process.*, 2024, **171**, 107989.
47 Y.-L. Liu, Y. Shi, H. Yin and C.-L. Yang, *Appl. Phys. Lett.*, 2020, **117**, 063901.
48 L. G. Du and S. D. Wang, *Appl. Surf. Sci.*, 2023, **614**, 156272.
49 M. Born, *On the stability of crystal lattices. I, Mathematical Proceedings of the Cambridge Philosophical Society*, Cambridge University Press, 1940, pp. 160–172.
50 A. Carvalho, M. Wang, X. Zhu, A. S. Rodin, H. Su and A. H. Castro Neto, *Nat. Rev. Mater.*, 2016, **1**, 1–16.
51 Z. Gao, X. Dong, N. Li and J. Ren, *Nano Lett.*, 2017, **17**, 772–777.
52 D. Carlstedt, E. Marklund and L. E. Asp, *Compos. Sci. Technol.*, 2019, **169**, 26–33.
53 J. Lou, K. Ren, Z. Huang, W. Huo, Z. Zhu and J. Yu, *RSC Adv.*, 2021, **11**, 29576–29584.
54 Q. Gao, C. Xia, W. Xiong, J. Du, T. Wang, Z. Wei and J. Li, *J. Mater. Chem. C*, 2017, **5**, 12629–12634.
55 E. Torun, H. Sahin and F. Peeters, *Phys. Rev. B*, 2016, **93**, 075111.
56 X. Cai, W. Chen, X. Jia, L. Zhang, Q. Wang, B. Wang, X. Yang, Y. Liu and Y. Jia, *J. Mater. Chem. C*, 2020, **8**, 12291–12301.
57 W. Tang, E. Sanville and G. Henkelman, *J. Phys.: Condens. Matter*, 2009, **21**, 084204.
58 J. Wang, N. Zhang, Y. Wang, H. Zhao, H. Chen, H. Zeng, L. Zhao, Q. Yang and B. Feng, *Int. J. Hydrogen Energy*, 2024, **53**, 247–255.
59 Z.-Q. Fan, X.-W. Jiang, J.-W. Luo, L.-Y. Jiao, R. Huang, S.-S. Li and L.-W. Wang, *Phys. Rev. B*, 2017, **96**, 165402.
60 S. Braun, W. R. Salaneck and M. Fahlman, *Adv. Mater.*, 2009, **21**, 1450–1472.
61 J. Liu, B. Cheng and J. Yu, *Phys. Chem. Chem. Phys.*, 2016, **18**, 31175–31183.
62 H. Zhao, E. Li, C. Liu, Y. Shen, P. Shen, Z. Cui and D. Ma, *Vacuum*, 2021, **192**, 110434.
63 Z. Cui, X. Gao, S. Zhang and L. Wang, *ChJPh*, 2024, **91**, 421–431.
64 Z. Cui, H. Meng, C. Zhang, L. Zhang, S. Zhang and L. Wang, *Mater. Sci. Semicond. Process.*, 2024, **182**, 108705.
65 L. Ju, X. Tang, J. Li, L. Shi and D. Yuan, *Appl. Surf. Sci.*, 2022, **574**, 151692.
66 C.-F. Fu, J. Sun, Q. Luo, X. Li, W. Hu and J. Yang, *Nano Lett.*, 2018, **18**, 6312–6317.
67 H. Qiao, Y. Zhang, Z.-H. Yan, L. Duan, L. Ni and J.-B. Fan, *Appl. Surf. Sci.*, 2022, **604**, 154602.
68 Y. Zhang, H. Qiao, Z.-H. Yan, L. Duan, L. Ni and J.-B. Fan, *Int. J. Hydrogen Energy*, 2023, **48**, 14659–14669.
69 H. Wenna, C. Xuefeng, J. Minglei, R. Fengzhu, P. Chengxiao, Y. Haigang, G. Qinfen, W. Bing and Y. Huabing, *J. Phys. D: Appl. Phys.*, 2022, **55**, 264001.
70 R. Zhang, F. Zhuang, R. Zhou, J. Ma, H. Li, K. Wang, X. Ye and G. Hao, *J. Phys. Chem. Solids*, 2022, **171**, 111014.
71 K.-X. Xie, Y. Zhang, Z.-B. Qiang, J.-X. Ding, H. Nouguiza, H.-X. Chen, L. Duan, J.-B. Fan and L. Ni, *Int. J. Hydrogen Energy*, 2024, **51**, 1381–1391.
72 H. Yang, Y. Ma, S. Zhang, H. Jin, B. Huang and Y. Dai, *J. Mater. Chem. A*, 2019, **7**, 12060–12067.
73 Z. Cui, H. Wang, Y. Shen, K. Qin, P. Yuan and E. Li, *Int. J. Hydrogen Energy*, 2024, **88**, 898–905.